Simulating One-Photon Absorption and Resonance Raman Scattering Spectra Using Analytical Excited State Energy Gradients within Time-Dependent Density Functional Theory

Daniel W. Silverstein,[†] Niranjan Govind,*[,‡] Hubertus J. J. van Dam,[‡] and Lasse Jensen*[,†]

[†]Department of Chemistry, The Pennsylvania State University, 104 Chemistry Building, University Park, Pennsylvania 16802, United States

[‡]William R. Wiley Environmental Molecular Sciences Laboratory, Pacific Northwest National Laboratory, 902 Battelle Boulevard, Richland, Washington 99352, United States

S *Supporting Information*

ABSTRACT: A parallel implementation of analytical time-dependent density functional theory gradients is presented for the quantum chemistry program NWChem. The implementation is based on the Lagrangian approach developed by Furche and Ahlrichs. To validate our implementation, we first calculate the Stokes shifts for a range of organic dye molecules using a diverse set of exchange-correlation functionals (traditional density functionals, global hybrids, and range-separated hybrids) followed by simulations of the one-photon absorption and resonance Raman scattering spectrum of the phenoxyl radical, the well-studied dye molecule rhodamine 6G, and a molecular host−guest complex (TTF⊂CBPQT⁴⁺). The study of organic dye molecules illustrates that B3LYP and CAM-B3LYP generally give the best agreement with experimentally determined Stokes shifts unless the excited state is a charge transfer state. Absorption, resonance Raman, and fluorescence simulations for the phenoxyl radical indicate that explicit solvation may be required for accurate characterization. For the host−guest complex and rhodamine 6G, it is demonstrated that absorption spectra can be simulated in good agreement with experimental data for most exchange-correlation functionals. However, because one-photon absorption spectra generally lack well-resolved vibrational features, resonance Raman simulations are necessary to evaluate the accuracy of the exchange-correlation functional for describing a potential energy surface.
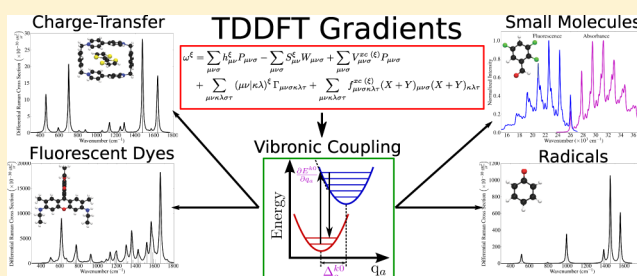
1. INTRODUCTION

The excited state properties of molecules lead to diverse applications,[1,2] including solution phase detection of molecular binding events,[3−5] photodynamic therapy,[6,7] and biological imaging.[8−10] A detailed understanding of molecule-radiation interactions often requires analysis of experimental data and applications of theory, which has been demonstrated by several groups.[11−15] Since its introduction[16] and implementation for molecular systems,[17,18] time-dependent density functional theory (TDDFT) has become a powerful approach to study low-lying valence excited states[19−25] as well as core-level excitations[26−31] efficiently and accurately.

Excited-state gradients, which are needed for spectroscopy simulations and the dynamics of photochemical processes can also be evaluated analytically at a computationally reasonable cost within the framework of TDDFT. Pioneering efforts by Amos et al. demonstrated the accuracy of TDDFT energy gradients for determining excited state geometries and dipoles using time-dependent Hartree−Fock (TDHF) and a variety of exchange-correlation (XC) functionals.[32−35] Furche and co-workers[36,37] introduced the Lagrangian formulation of the excitation energy, enabling efficient calculation of excited state

properties at costs comparable to the ground state gradient. Hutter et al. employed this framework for TDDFT gradients within the plane wave basis formalism.[38,39] Seth et al. extended the Lagrangian formulation for Slater-type orbitals and spin-flip TDDFT,[40] and Petrenko et al. implemented the expressions for including frozen core orbitals and chain of spheres exchange.[41] Extensions of the Lagrangian formulation of TDDFT gradients have also been devised to include range separated XC functionals,[42,43] the Tamm-Dancoff approximation,[44] molecular-orbital free implementations,[45] and environmental effects including continuum[46,47] and explicit solvent models.[48,49] Although the Lagrangian approach is widely used, TDDFT gradients have also been developed employing implicit differentiation,[50] Green's function methods,[51] and real-space TDDFT.[52]

Analytical excited state gradients are also useful for describing vibronic features for one-photon absorption (OPA) and resonance Raman scattering spectra.[53−57] Raman scattering is an inelastic light scattering process, where radiation with

frequency ω_L is absorbed, and then radiation is scattered with frequency $\omega_s = \omega_L - \omega_v$, with ω_v corresponding to a vibrational frequency of the molecule. When ω_L is tuned to an electronic excitation energy, resonance enhancement is observed, and the process is called resonance Raman scattering (RRS). Vibrational information that is coupled to an electronic transition is therefore obtained by this method. RRS has been demonstrated as a valuable technique in characterizing fluorescent dyes,[58−61] biomolecules,[62−64] and photon-induced electron transfer processes.[11,65−68]

In this work, we present our parallel implementation of analytical TDDFT excitation energy gradients based on the Lagrangian formalism of Furche and Ahlrichs[36] in the NWChem quantum chemistry program.[69] We also present the utility of TDDFT excitation energy gradients to determine the Stokes shifts for a set of organic dyes, and by combining the excitation energy gradients with a time-dependent wavepacket formalism,[70−75] we demonstrate how OPA and RRS can be simulated efficiently for fluorescent dyes and charge-transfer complexes.[53] The rest of the paper is organized as follows. In section 2, we outline the theory for the Lagrangian formalism for excitation energy gradients and its application toward obtaining vibronic coupling parameters. The computational details are presented in section 3. Finally, in section 4 we present and discuss features of our implementation based simulations of optical properties for organic dyes, radicals, and molecules with charge-transfer states using several XC functionals.

2. THEORY

2.1. Analytical Excitation Energy Gradients with TDDFT.
In this section, we present the key expressions in the derivation of gradients of the excitation energy using TDDFT based on the original derivation in ref 36. The TDDFT equations can be written as follows:

$$
\begin{aligned}
G[\mathbf{X}, \mathbf{Y}, \omega] = \frac{1}{2} & [(\mathbf{X} + \mathbf{Y})^T (\mathbf{A} + \mathbf{B})(\mathbf{X} + \mathbf{Y}) \\
& + (\mathbf{X} - \mathbf{Y})^T (\mathbf{A} - \mathbf{B})(\mathbf{X} - \mathbf{Y})] \\
& - \omega[(\mathbf{X} + \mathbf{Y})^T (\mathbf{X} - \mathbf{Y}) - 1] \\
= \frac{1}{2} & \sum_{ia\sigma jb\tau} [(X + Y)_{ia\sigma}(A + B)_{ia\sigma jb\tau}(X + Y)_{jb\tau} \\
& + (X - Y)_{ia\sigma}(A - B)_{ia\sigma jb\tau}(X - Y)_{jb\tau}] \\
& - \omega \Big[\sum_{ia\sigma} (X + Y)_{ia\sigma}(X - Y)_{ia\sigma} - 1\Big]
\end{aligned}
\tag{1}
$$

In eq 1, the matrices $(\mathbf{A} + \mathbf{B})$ and $(\mathbf{A} - \mathbf{B})$, which are sometimes called orbital rotation Hessians, have the following matrix representation

$$
\begin{aligned}
(A + B)_{ia\sigma jb\tau} = {} & \delta_{\sigma\tau}\delta_{ab}\delta_{ij}(\varepsilon_{a\sigma} - \varepsilon_{i\sigma}) + 2(ia\sigma|jb\tau) + 2f^{xc}_{ia\sigma jb\tau} \\
& - c_x \delta_{\sigma\tau}[(ab\sigma|ij\sigma) + (ja\sigma|ib\sigma)]
\end{aligned}
\tag{2}
$$

and

$$
\begin{aligned}
(A - B)_{ia\sigma jb\tau} = {} & \delta_{\sigma\tau}\delta_{ab}\delta_{ij}(\varepsilon_{a\sigma} - \varepsilon_{i\sigma}) + c_x \delta_{\sigma\tau}[(ja\sigma|ib\sigma) \\
& - (ab\sigma|ij\sigma)]
\end{aligned}
\tag{3}
$$

In eqs 2 and 3, $f^{xc}_{\sigma\tau}$ is the XC kernel

$$
f^{xc}_{\sigma\tau} = \frac{\delta^2 E^{xc}}{\delta\rho_\sigma(\mathbf{r}') \, \delta\rho_\tau(\mathbf{r})}
\tag{4}
$$

For all quantities, indices i, j, k, l, ... indicate occupied orbitals; a, b, c, d, ... are virtual (unoccupied) orbitals; σ, τ, and v are spin indices; and p, q, r, s, ... are arbitrary orbitals. The molecular orbital (MO) energies are $\varepsilon_{p\sigma}$, the percentage of the Hartree−Fock (HF) exchange is given by c_x, and the two-electron integrals are written in Mulliken notation. Upon solving the TDDFT equations, the excitation energy ω and excitation vectors (sometimes called configuration interaction (CI) vectors) $\mathbf{X}$ and $\mathbf{Y}$ are obtained.

The derivation of TDDFT gradients depends on the evaluation of the Lagrangian functional given by

$$
\begin{aligned}
L[&\mathbf{X}, \mathbf{Y}, \omega, \mathbf{C}, \mathbf{Z}, \mathbf{W}] \\
= \frac{1}{2} & \sum_{ia\sigma jb\tau} [(X + Y)_{ia\sigma}(A + B)_{ia\sigma jb\tau}(X + Y)_{jb\tau} \\
& + (X - Y)_{ia\sigma}(A - B)_{ia\sigma jb\tau}(X - Y)_{jb\tau}] \\
& - \omega \Big[\sum_{ia\sigma} (X + Y)_{ia\sigma}(X - Y)_{ia\sigma} - 1\Big] + \sum_{ia\sigma} Z_{ia\sigma} F_{ia\sigma} \\
& - \sum_{pq\sigma, p \leq q} W_{pq\sigma}(S_{pq\sigma} - \delta_{pq}) \\
= G&[X, Y, \omega] + \sum_{ia\sigma} Z_{ia\sigma} F_{ia\sigma} - \sum_{pq\sigma, p \leq q} W_{pq\sigma}(S_{pq\sigma} - \delta_{pq})
\end{aligned}
\tag{5}
$$

The Lagrangian functional L depends on the excitation energy and excitation vectors, the MO coefficients $\mathbf{C}$, and Lagrange multipliers $\mathbf{Z}$ and $\mathbf{W}$. In eq 5, $F_{pq\sigma}$ and $S_{pq\sigma}$ are the Fock and overlap matrices, respectively. The Fock matrix is defined as

$$
F_{pq\sigma} = h_{pq\sigma} + \sum_{i\tau} [(pq\sigma|ii\tau) - c_x \delta_{\sigma\tau}(pi\sigma|iq\sigma)] + V^{xc}_{pq\sigma}
\tag{6}
$$

In eq 6, h is the core Hamiltonian, the second term is the Coulomb integral, the third term is the HF exchange contribution, and the last term, the XC potential, is given by

$$
V^{xc}_{pq\sigma} = \langle p\sigma|V^{xc}_\sigma|q\sigma \rangle = \int dr \, \phi_{p\sigma}(r) \frac{\delta E^{xc}}{\delta\rho_\sigma(r)} \phi_{q\sigma}(r)
\tag{7}
$$

where $\phi_{p\sigma}$ is a MO. The Lagrange multipliers enforce two constraints:

1. $\mathbf{Z}$ enforces that the ground state Kohn−Sham (KS) equation has been solved.
2. $\mathbf{W}$ enforces that the MOs are orthonormal.

The Lagrange multipliers ensure that the Lagrangian functional is forced to obey the variational principle. In other words, the Lagrangian functional is stationary with respect to changes in the MO coefficients:

$$
\frac{\partial L}{\partial C_{\mu p\sigma}} = 0 = \frac{\partial G}{\partial C_{\mu p\sigma}} + \sum_{ia\tau} Z_{ia\tau} \frac{\partial F_{ia\tau}}{\partial C_{\mu p\sigma}} - \sum_{rs\tau, r \leq s} W_{rs\tau} \frac{\partial S_{rs\tau}}{\partial C_{\mu p\sigma}}
\tag{8}
$$

The most significant consequence of eq 8 is that derivatives of the Lagrangian functional with respect to geometric perturbations or external fields (for polarizabilities) can be evaluated by keeping the MO coefficients fixed at the ground state optimized values. This enables gradients of the excitation energy to be

calculated at a cost comparable to a ground state energy gradient. Evaluation of eq 8 is required to determine the Lagrange multipliers and makes frequent use of the transformation from atomic orbital (AO) indices (μ, ν, λ, κ, ...) to MO indices. For an arbitrary quantity $V_{pq\sigma}$, this transformation can be written as

$$V_{pq\sigma} = \sum_{\mu\nu} C_{\mu p\sigma} V_{\mu\nu\sigma} C_{\nu q\sigma} \tag{9}$$

The derivatives on the right-hand side of eq 8 can be evaluated by employing the definitions of $G[\mathbf{X},\mathbf{Y},\omega]$, the Fock matrix, and overlap matrix. For the Fock and overlap matrices, the expressions are given by

$$\sum_{ia\tau} Z_{ia\tau} \sum_{\mu} \frac{\partial F_{ia\tau}}{\partial C_{\mu q\sigma}} C_{\mu q\sigma}$$
$$= \sum_{ia\tau} (\delta_{\sigma\tau}\delta_{ip}\delta_{qa} + \delta_{\sigma\tau}\delta_{ap}\delta_{iq})\varepsilon_{q\sigma} Z_{ia\tau} + \sum_{j} \delta_{jp} H^{+}_{pq\sigma}[\mathbf{Z}] \tag{10}$$

$$\sum_{\mu} \sum_{rs\tau, r\leq s} W_{rs\tau} \frac{\partial S_{rs\tau}}{\partial C_{\mu p\sigma}} C_{\mu q\sigma} = (1 + \delta_{pq}) W_{pq\sigma} \tag{11}$$

For the functional $G[\mathbf{X},\mathbf{Y},\omega]$, the derivatives of the orbital rotation Hessians with respect to the MO coefficients are required.

$$Q_{pq\sigma} = \sum_{\mu} \frac{\partial G[\mathbf{X}, \mathbf{Y}, \omega]}{\partial C_{\mu p\sigma}} C_{\mu q\sigma}$$
$$= \frac{1}{2} \sum_{kc\tau ld\upsilon} (X + Y)_{kc\tau} \left\{ \sum_{\mu} \frac{\partial}{\partial C_{\mu p\sigma}}[(A + B)_{kc\tau ld\upsilon}] \right.$$
$$\times \left. C_{\mu q\sigma} \right\}(X + Y)_{ld\upsilon} + \frac{1}{2} \sum_{kc\tau ld\upsilon} (X - Y)_{kc\tau}$$
$$\times \left\{ \sum_{\mu} \frac{\partial}{\partial C_{\mu p\sigma}}[(A - B)_{kc\tau ld\upsilon}] C_{\mu q\sigma} \right\}(X - Y)_{ld\upsilon} \tag{12}$$

These derivatives lead to lengthy expressions but may be simplified by looking at different blocks of the matrix $Q_{pq\sigma}$. For the occupied–occupied block ($p = i \leq q = j$), occupied–virtual block ($p = i$ and $q = a$), virtual–occupied block ($p = a$ and $q = i$), and virtual–virtual block ($p = a \leq q = b$), the expressions become

$$Q_{ij\sigma} = \omega \sum_{a} \{(X + Y)_{ia\sigma}(X - Y)_{ja\sigma} + (X - Y)_{ia\sigma}$$
$$\times (X + Y)_{ja\sigma}\} - \sum_{a} \varepsilon_{a\sigma}\{(X + Y)_{ia\sigma}(X + Y)_{ja\sigma}$$
$$+ (X - Y)_{ia\sigma}(X - Y)_{ja\sigma}\} + H^{+}_{ij\sigma}[\mathbf{T}]$$
$$+ 2 \sum_{kc\tau ld\upsilon} [g^{xc}_{ij\sigma kc\tau ld\upsilon}](X + Y)_{kc\tau}(X + Y)_{ld\upsilon} \tag{13}$$

$$Q_{ia\sigma} = H^{+}_{ia\sigma}(\mathbf{T}) + \sum_{b} \{(X + Y)_{ib\sigma} H^{+}_{ab\sigma}[(\mathbf{X} + \mathbf{Y})]$$
$$+ (X - Y)_{ib\sigma} H^{-}_{ab\sigma}[(\mathbf{X} - \mathbf{Y})]\}$$
$$+ 2 \sum_{kc\tau ld\upsilon} [g^{xc}_{ia\sigma kc\tau ld\upsilon}](X + Y)_{kc\tau}(X + Y)_{ld\upsilon} \tag{14}$$

$$Q_{ai\sigma} = \sum_{j} \{(X + Y)_{ja\sigma} H^{+}_{ji\sigma}[(X + Y)]$$
$$+ (\mathbf{X} - \mathbf{Y})_{ja\sigma} H^{-}_{ji\sigma}[(\mathbf{X} - \mathbf{Y})]\} \tag{15}$$

$$Q_{ab\sigma} = \omega \sum_{i} \{(X + Y)_{ia\sigma}(X - Y)_{ib\sigma} + (X - Y)_{ia\sigma}$$
$$\times (X + Y)_{ib\sigma}\} + \sum_{i} \varepsilon_{b\sigma}\{(X + Y)_{ia\sigma}(X + Y)_{ib\sigma}$$
$$+ (X - Y)_{ia\sigma}(X - Y)_{ib\sigma}\} \tag{16}$$

The linear transformations are

$$H^{+}_{pq\sigma}[\mathbf{V}] = \sum_{rs\tau} [2(rs\tau|qp\sigma) + 2f^{xc}_{pq\sigma rs\tau} - c_x\delta_{\sigma\upsilon}[(rq\upsilon|ps\upsilon)$$
$$+ (rp\upsilon|qs\upsilon)]]V_{rs\tau} \tag{17}$$

$$H^{-}_{pq\sigma}[V] = \sum_{rs\tau} \{[c_x\delta_{\sigma\tau}[(rq\sigma|ps\sigma) - (qs\sigma|pr\sigma)]]\}V_{rs\tau} \tag{18}$$

where the vector $\mathbf{T}$ is the unrelaxed one-particle difference density matrix, defined as

$$T_{ab\tau} = \frac{1}{2} \sum_{i} \{(X + Y)_{ia\tau}(X + Y)_{ib\tau}$$
$$+ (X - Y)_{ia\tau}(X - Y)_{ib\tau}\} \tag{19}$$

$$T_{ij\tau} = -\frac{1}{2} \sum_{a} \{(X + Y)_{ia\tau}(X + Y)_{ja\tau}$$
$$+ (X - Y)_{ia\tau}(X - Y)_{ja\tau}\} \tag{20}$$

$$T_{ia\tau} = T_{ai\tau} = 0 \tag{21}$$

and the third derivative of the XC functional is

$$g^{xc}_{\sigma\tau\upsilon} = \frac{\delta^3 E^{xc}}{\delta\rho_\sigma(r)\,\delta\rho_\tau(\mathbf{r'})\,\delta\rho_\upsilon(\mathbf{r''})} \tag{22}$$

By combining eqs 13 through 16 with eqs 10 and 11, four linear equations are obtained that enable the Lagrange multipliers $\mathbf{Z}$ and $\mathbf{W}$ to be determined.

$$Q_{ij\sigma} + H^{+}_{ij\sigma}[\mathbf{Z}] = (1 + \delta_{ij})W_{ij\sigma} \tag{23}$$

$$Q_{ia\sigma} + \varepsilon_{a\sigma}Z_{ia\sigma} + H^{+}_{ia\sigma}[\mathbf{Z}] = W_{ia\sigma} \tag{24}$$

$$Q_{ai\sigma} + \varepsilon_{i\sigma}Z_{ia\sigma} = W_{ia\sigma} \tag{25}$$

$$Q_{ab\sigma} = (1 + \delta_{ab})W_{ab\sigma} \tag{26}$$

Taking the difference between eqs 24 and 25, it is possible to evaluate $\mathbf{Z}$

$$\sum_{jb\tau} (A + B)_{ia\sigma jb\tau} Z_{jb\tau} = -R_{ia\sigma} \tag{27}$$

where the right-hand side vector is

$$R_{ia\sigma} = H_{ia\sigma}^+[\mathbf{T}] + \sum_b \{(X+Y)_{ib\sigma}H_{ab\sigma}^+[(\mathbf{X}+\mathbf{Y})]$$
$$+ (X-Y)_{ib\sigma}H_{ab\sigma}^-[(\mathbf{X}-\mathbf{Y})]\}$$
$$+ 2\sum_{kc\tau ld\upsilon}[g_{ia\sigma kc\tau ld\upsilon}^{xc}](X+Y)_{kc\tau}(X+Y)_{ld\upsilon}$$
$$- \sum_j \{(X+Y)_{ja\sigma}H_{ji\sigma}^+[(\mathbf{X}-\mathbf{Y})]$$
$$+ (X+Y)_{ja\sigma}H_{ji\sigma}^-[(\mathbf{X}-\mathbf{Y})]\} \tag{28}$$

The Lagrange multiplier $\mathbf{W}$ can be evaluated after we obtain $\mathbf{Z}$

$$W_{ij\sigma} = \frac{1}{1+\delta_{ij}}(Q_{ij\sigma} + H_{ij\sigma}^+[\mathbf{Z}]) \tag{29}$$

$$W_{ab\sigma} = \frac{1}{1+\delta_{ab}}Q_{ab\sigma} \tag{30}$$

$$W_{ia\sigma} = Q_{ai\sigma} + \varepsilon_{i\sigma}Z_{ia\sigma} \tag{31}$$

With $\mathbf{Z}$ and $\mathbf{W}$, the gradient of the Lagrangian can be evaluated to obtain the gradient of the excitation energy. The expression for the gradient of the excitation energy is

$$\omega^\xi = \sum_{\mu\nu\sigma} h_{\mu\nu}^\xi P_{\mu\nu\sigma} - \sum_{\mu\nu\sigma} S_{\mu\nu}^\xi W_{\mu\nu\sigma}$$
$$+ \sum_{\mu\nu\sigma} V_{\mu\nu\sigma}^{xc(\xi)}P_{\mu\nu\sigma} + \sum_{\mu\nu\kappa\lambda\sigma\tau}(\mu\nu|\kappa\lambda)^\xi \Gamma_{\mu\nu\sigma\kappa\lambda\tau}$$
$$+ \sum_{\mu\nu\kappa\lambda\sigma\tau} f_{\mu\nu\sigma\kappa\lambda\tau}^{xc(\xi)}(X+Y)_{\mu\nu\sigma}(X+Y)_{\kappa\lambda\tau} \tag{32}$$

The superscript, ξ, indicates the derivative of a quantity with respect to a nuclear coordinate. When written as (ξ), this indicates that the derivative is taken with respect to a nuclear coordinate with the MO coefficients held fixed at their ground state values. This is a consequence of the density functional theory (DFT) contributions to the gradients implicitly depending on the MO coefficients. Here, two new quantities are defined, the relaxed one-particle difference density matrix ($\mathbf{P} = \mathbf{T} + \mathbf{Z}$) and the effective two-particle difference density matrix $\Gamma_{\mu\nu\sigma\kappa\lambda\tau}$, defined as

$$\Gamma_{\mu\nu\sigma\kappa\lambda\tau} = \frac{1}{2}\{2(X+Y)_{\mu\nu\sigma}(X+Y)_{\kappa\lambda\tau} + 2P_{\mu\nu\sigma}D_{\kappa\lambda\tau}$$
$$- c_x\delta_{\sigma\tau}[P_{\mu\kappa\sigma}D_{\nu\lambda\tau} + P_{\mu\lambda\sigma}D_{\nu\kappa\tau} + (X+Y)_{\kappa\nu\sigma}$$
$$\times (X+Y)_{\mu\lambda\tau} + (X+Y)_{\kappa\mu\sigma}(X+Y)_{\lambda\nu\tau}$$
$$- (X-Y)_{\kappa\nu\sigma}(X-Y)_{\mu\lambda\tau} + (X-Y)_{\kappa\mu\sigma}$$
$$\times (X-Y)_{\lambda\nu\tau}]\} \tag{33}$$

The expressions in this section were implemented into the NWChem quantum chemistry program.[69] Evaluation of eqs 28 and 32 require third order functional derivatives, which were derived, implemented, and tested using numerical differentiation of second order derivatives. Several types of XC functionals are included in the implementation: the local density approximation (LDA), generalized gradient approximation (GGA), global hybrids, and range-separated hybrids. A complete list of the functionals is included in Table 1. Both full linear response TDDFT and the Tamm-Dancoff approximation

Table 1. Definitions of the XC Functionals[a]

functional	definition
LDA	Slater + VWN 5
BP86	Becke 88 + Perdew 86
PBE	PBEx + PBEc
BLYP	Becke 88 + LYP
B3LYP	Slater (80%) + Becke 88 (nonlocal, 72%) + HF Exchange (20%) + LYP (81%) + VWN 1 RPA (19%)
PBE0	PBEx (75%) + HF Exchange (25%) + PBEc
BHLYP	Slater (50%) + Becke 88 (nonlocal, 50%) + HF Exchange (50%) + LYP
CAM-B3LYP	CAM-Becke 88 ($\alpha = 0.19$, $\beta = 0.46$, $\omega = 0.33$) + LYP
LC-PBE	CAM-PBE ($\alpha = 0.00$, $\beta = 1.00$, $\omega = 0.30$) + PBEc
LC-PBE0	CAM-PBE ($\alpha = 0.25$, $\beta = 0.75$, $\omega = 0.30$) + PBEc
BNL	Baer−Neuhauser−Livshits ($\alpha = 0.00$, $\beta = 1.00$, $\omega = 0.33$) + LYP
LC-ωPBE	LC-ωPBE ($\alpha = 0.00$, $\beta = 1.00$, $\omega = 0.30$) + PBEc
LC-ωPBEh	LC-ωPBE ($\alpha = 0.20$, $\beta = 0.80$, $\omega = 0.20$) + PBEc
LC-BLYP	CAM-Becke 88 ($\alpha = 0.00$, $\beta = 1.00$, $\omega = 0.33$) + LYP

[a]The table is separated between the local and semilocal functionals, global hybrids, and long-range corrected hybrids. For the latter, we report the α, β, and ω parameters.

(TDA) can be used to evaluate gradients for restricted singlet, restricted triplet, and unrestricted calculations.

2.2. Calculating Vibronic Coupling Parameters. The vibronic coupling parameters (dimensionless displacements) are related to the gradient of the excited state energy (E^{0k}, which is equivalent to ω from section 2.1) along normal mode Q_a. This is shown in Figure 1. In this section, the normal mode
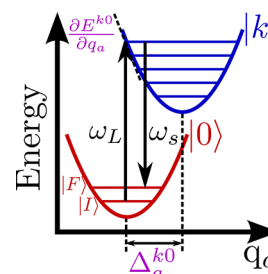

Figure 1. A depiction of the independent-mode displaced harmonic oscillator model, assuming a resonance Raman scattering process. Here, ω_L is the incident frequency of light, ω_s is the scattered frequency of light, and Δ_a^{0k} is the dimensionless displacement of normal mode q_a.

in mass-weighted units is written as Q_a, while it is written as q_a for normal (dimensionless) coordinates. On the basis of approximations where the ground and excited state potential energy surfaces are harmonic and that there is no change in the normal-mode frequencies when the ground and excited states are compared (i.e., no Duschinsky rotations[76]), the dimensionless displacements are calculated as

$$V_{q_a} = \left(\frac{\partial E^{0k}}{\partial q_a}\right)_{q_a = 0} = -\omega_{a0}\Delta_a^{0k} \tag{34}$$

where ω_{a0} is the normal-mode frequency and Δ_a^{0k} is the dimensionless displacement of mode q_a for the nth excited state. In general, it is simpler to evaluate the gradient with respect to Q_a more directly. This requires an additional step,[77]

$$\frac{\partial E^{0k}}{\partial q_a} = \left(\frac{dQ_a}{dq_a}\right)\frac{\partial E^{0k}}{\partial Q_a} = \sqrt{\frac{\hbar}{2\pi c \nu_{a0}}}\frac{\partial E^{0k}}{\partial Q_a} = \sqrt{\frac{\hbar}{2\pi c \nu_{a0}}}V_{Q_a}$$

$$(35)$$

The only variability in this expression is how the excited state gradient in terms of mass-weighted coordinates V_{Q_a} is evaluated. It has been demonstrated previously that numerical gradients can be used for vibronic simulations of spectroscopy.[15,78–83] Other research groups have employed analytical gradients of the excited state.[53,54] Numerical gradients of the excitation energy require finite differentiation, where excitation energies are calculated by stepping in the positive and negative directions along the normal modes.

2.2.1. Numerical Excited State Energy Gradients. The numerical evaluation of excited state energy gradients revolves around calculating the linear response of a molecule up to a particular excitation. For any molecule, there are $3N - 5$ or $3N - 6$ (N is the number of atoms) normal modes. Performing a numerical evaluation of the excited state energy gradient requires either $6N - 10$ or $6N - 12$ calculations, because this requires calculations of the excitation energy in the positive and negative directions along every normal mode. This can be reduced significantly by focusing on a portion of the normal modes in a wavenumber region.

For numerical evaluation of the excited state gradients, formulas analogous to those discussed by Reiher et al.[84] for the derivatives of the polarizability along normal mode Q_a are used, substituting the excitation energy in place of the polarizability. These derivatives are expressed using a three-point central differences formula as

$$\left(\frac{\partial E^{0n}}{\partial Q_a}\right)_{Q_a=0} = \frac{E^{0k}(\mathbf{R}_{eq} + s_R\mathbf{R}_a) - E^{0k}(\mathbf{R}_{eq} - s_R\mathbf{R}_a)}{2s_{Q_a}|\mathbf{Q}_a^{norm}|}$$

$$(36)$$

In eq 36, $\mathbf{R}_{eq}$ is a vector of the optimized coordinates of the molecule's ground state, $\mathbf{R}_a$ is the Cartesian normal mode vector, s_R is the Cartesian step size (typically 0.01 is used), and $|\mathbf{Q}_a^{norm}|$ is the norm of the normalized mass-weighted normal mode vector. The latter quantity is used to give the equation appropriate dimensions but is clearly equal to one. In this expression, s_{Q_a} is

$$s_{Q_a} = \frac{s_R}{|\mathbf{R}_a|} = s_R\left[\sum_{i=1}^{3N}\frac{(Q_{a,i}^{norm})^2}{m_i}\right]^{-1/2}$$

$$(37)$$

Either the expression in the middle or the right side may be used to find s_{Q_a} depending on whether the normalized mass-weighted normal mode vector $\mathbf{Q}_a$ or the unnormalized Cartesian normal mode vector $\mathbf{R}_a$ is available. If the normalized mass-weighted normal mode vector is used, each squared component is divided by the mass of the ith atom (m_i).

2.2.2. Analytical Excited State Energy Gradients. If analytical geometry optimizations are available in a quantum chemistry program, a significant advantage can be gained in calculating the dimensionless displacements. In the numerical method described above, the majority of the time spent involves the $6N - 10$ or $6N - 12$ calculations to obtain all of the simulation parameters. In general, for all but the smallest molecules, collection of that data requires substantial amounts of computer time. Analytical gradients of the excited state

energy, which come from performing an analytical excited state geometry optimization, are used to determine the dimensionless displacements and only require one calculation. A side-by-side comparison of the numerical and analytical methods shows that if you account for the redundant calculations (the ground state geometry optimization and normal-mode analysis), the analytical approach results in a significant reduction in both CPU and wall time. This speedup results from analytical gradients requiring roughly the same computational effort as a ground state gradient calculation,[36] which can decrease the computation time by 2 orders of magnitude as we have shown.[85]

The analytical method involves two different techniques: analytical excited state geometry optimization (method I) and analytical excited state gradients at the ground state equilibrium position (method II). We will focus on method II here. For method II, the dimensionless displacement is calculated by projecting the gradient of the excited state energy at the ground state equilibrium position onto the normal modes. This method is written as

$$V_{Q_a} = \sum_i \frac{1}{\sqrt{m_i}}V_{X,i}L_{ia}$$

$$(38)$$

where m_i is the mass of the atom corresponding to component i and $V_{X,i}$ is the Cartesian excited state energy gradient at the ground state equilibrium position. This is obtained from the first cycle of the excited state geometry optimization, assuming that the ground state equilibrium geometry is the starting point of that optimization. From the gradient V_{Q_a}, the dimensionless displacement is calculated using eq 34.

3. COMPUTATIONAL DETAILS

In Table 1, we present the definitions of all the XC functionals that are available with our analytic TDDFT gradients implementation and the ones used in this work. For the long-range (LC) corrected XC functionals, we use the following definition:

$$\frac{1}{r_{12}} = \frac{1 - [\alpha + \beta\,\text{erf}(\omega r_{12})]}{r_{12}} + \frac{\alpha + \beta\,\text{erf}(\omega r_{12})}{r_{12}}$$

$$(39)$$

where r_{12} is the electronic separation, ω is the attenuation parameter, α is a parameter allowing the incorporation of HF exchange, and β is a parameter allowing for the incorporation of DFT exchange, with the requirements $0 \le \alpha \le 1$, $0 \le \beta \le 1$, and $0 \le \alpha + \beta \le 1$ being satisfied.

As mentioned earlier, geometry optimizations, normal-mode analysis, and excited state energy gradient calculations were performed in a development version of the NWChem quantum chemistry program,[69] while the OPA and RRS simulations were performed using a locally developed program, TDSPEC.[86]

For the simulations presented in section 4.1, the organic dye molecules were optimized in the ground and excited states using the BLYP, LC-BLYP, B3LYP, and CAM-B3LYP XC functionals with the 6-31G* basis set. In section 4.3, the host–guest complex was optimized in its ground state, and vibrational frequencies were determined using B3LYP with dispersion corrections through the DFT-D2 method[87] and 6-311G* basis set. Excitation energy gradients were then determined using the B3LYP and LC-ωPBE functionals to simulate OPA and RRS. Results in section 4.4 for rhodamine 6G are based on the ground state optimized geometry and vibrational frequencies using B3LYP/6-311G*. All normal-mode frequencies are scaled
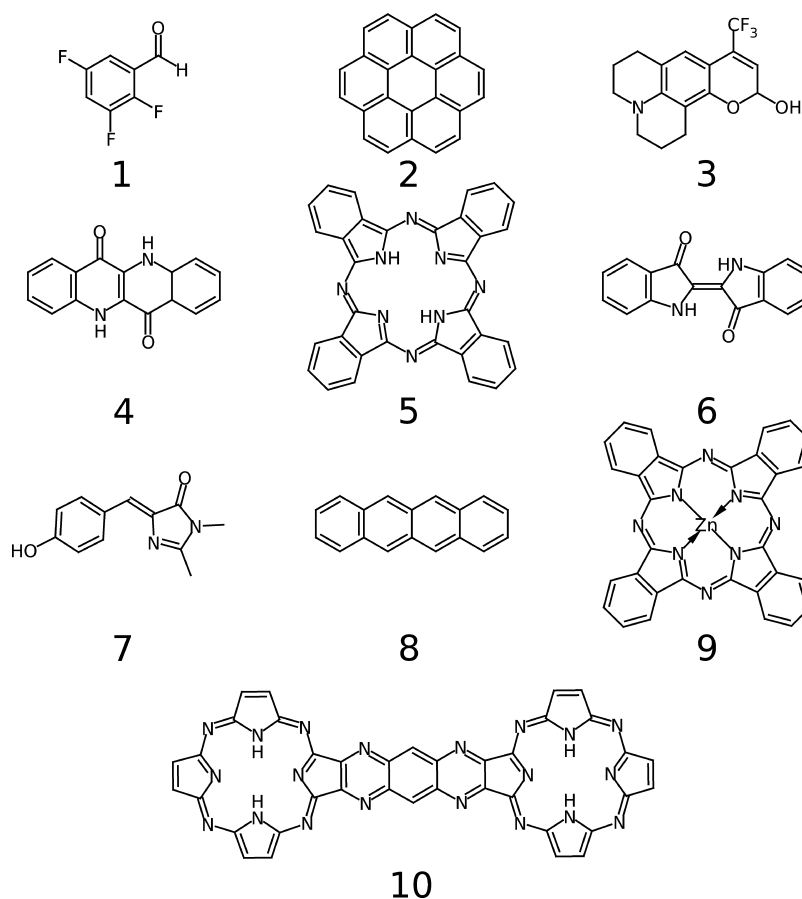
Figure 2. Structures of organic dye molecules used in this work. The numbered dyes correspond to those presented in Table 2.

Table 2. Absorption Maxima, Emission Maxima, and Stokes Shifts (S.S.) for a Test Set of Dye Molecules Using BLYP, LC-BLYP, B3LYP, and CAM-B3LYP Using the 6-31G* Basis Set[a]

|	BLYP			LC-BLYP			B3LYP			CAM-B3LYP			exp.
dye	Abs.	Em.	S.S.	Abs.	Em.	S.S.	Abs.	Em.	S.S.	Abs.	Em.	S.S.	S.S.
1	3.09	2.12	0.97	3.72	3.04	0.68	3.55	2.72	0.83	3.79	3.07	0.72	0.86[b]
2	3.68	3.62	0.06	5.00	4.79	0.21	4.16	4.06	0.10	4.73	4.56	0.17	0.23[c]
3	2.84	2.16	0.68	4.00	3.54	0.46	3.36	2.85	0.51	3.85	3.48	0.37	0.44[d]
4	2.63	2.49	0.14	3.71	3.34	0.37	3.11	2.90	0.21	3.58	3.26	0.32	0.19[e]
5	1.94	1.87	0.07	1.97	1.77	0.20	2.09	2.01	0.08	2.08	1.94	0.14	0.02[f]
6	1.99	1.26	0.73	2.70	2.45	0.25	2.31	2.09	0.22	2.64	2.41	0.23	0.10[e]
7	3.16	(I)	–	3.97	3.31	0.66	3.54	2.93	0.61	3.88	3.29	0.59	0.68[g]
8	2.14	1.90	0.14	3.15	2.60	0.55	2.49	2.16	0.33	2.78	2.45	0.33	0.36[h]
9	1.94	1.89	0.05	1.96	1.83	0.13	2.09	2.02	0.07	2.07	1.97	0.10	0.02[f]
10	1.47	1.29	0.18	1.97	1.94	0.03	1.94	1.76	0.18	2.13	2.11	0.02	–
ME			0.07			0.08			0.01			0.02	
MAE			0.18			0.10			0.06			0.08	
RMSD			0.26			0.12			0.07			0.09	

[a]Values are given in eV. Instabilities in the optimized excited state are labeled (I). Mean errors (ME), mean absolute errors (MAE), and root mean square deviations (RMSD) are reported in eV in comparison to experiment. [b]Reference 93. See text for discussion. [c]Reference 94. [d]Reference 95. [e]Reference 96. [f]Reference 100. [g]References 97 and 98. [h]Reference 99.

by 0.98 to account for anharmonicity in the normal modes and limitations of the basis set.[88−91]

4. RESULTS AND DISCUSSION

The results presented in this section show applications of the analytical excitation energy gradient implementation to a set of selected systems. Section 4.1 highlights the available excited state geometry optimization code for several types of XC functionals to determining accurate Stokes shifts. Sections 4.2−4.4 use the excited state energy gradients to evaluate vibronic coupling parameters, illustrating the capabilities of the code for studying radicals, molecules with charge-transfer excitations, and fluorescent dyes. In section 4.5, the timings of the current development version of the TDDFT gradient code are shown.
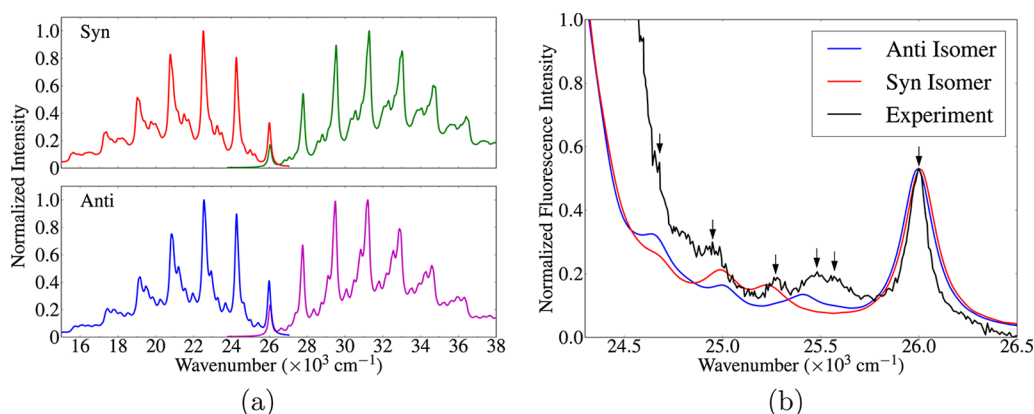
Figure 3. (a) Absorption (green and violet lines) and fluorescence (red and blue lines) spectra from 2,3,5-trifluorobenzaldehyde in the syn and anti conformations. (b) Simulated fluorescence spectra of the syn and anti conformations compared with the experimental fluorescence spectrum.[93] Results are calculated with B3LYP/aug-cc-pVTZ.

4.1. Absorption and Emission by Organic Dyes. In this section, we investigate the dependence of Stokes shifts on the XC functional for 10 organic chromophores. The test set includes the chromophores used in ref 92, which are illustrated in Figure 2. Dye molecules 1−6, 8, and 9 have experimentally measured absorption and fluorescence spectra in the gas phase, allowing a direct comparison of the Stokes shifts with the calculated results. Dye 7 (4′-hydroxybenzylidene-2,3-dimethy-limidazoline) is a model of the chromophore in green fluorescent protein and only has available absorption and fluorescent data in the protein environment.[97,98] While the simulations presented here neglect environmental effects, such as implicit or explicit solvation, this only has a small effect on the results presented in this section. It should be stressed that in situations where simulated results are compared with experiments measured in polar solvents or where environmental interactions are important, solvation effects generally must be included for accurate results.[46,101,102] Table 2 presents the calculated absorption and emission maxima along with Stokes shifts in comparison to the measured results. All excited state geometry optimizations were performed for the lowest energy strongly allowed excitation. This usually corresponded to the S_1 state of the chromophore.

The experimentally measured Stokes shifts span values ranging between nearly coincident absorption and emission maxima (free pthalocyanine, dye 5) to large shifts of ∼0.80 eV (2,3,5-trifluorobenzaldehyde, dye 1). In general, DFT captures the correct magnitudes of the Stokes shifts but is sensitive to the choice of XC functional. The BLYP functional, on average, yields the worst agreement with experimental measurements with a mean absolute error (MAE) of 0.18 eV and root-mean-square deviation (RMSD) of 0.26 eV. Inclusion of 20% HF with the B3LYP functional improves the results substantially with a MAE of 0.07 eV and RMSD of 0.08 eV. The range separated hybrid CAM-B3LYP yields comparable performance with B3LYP, while LC-BLYP (which includes 100% HF exchange at large interelectronic separation) slightly worsens the agreement with experimental results (MAE = 0.10 eV and RMSD = 0.12 eV). It is suggested through these results that HF exchange is required to improve the calculation of excited state properties in these systems.

In general, the Stokes shift is best described by the global hybrid B3LYP for the test set presented here. However, dye 2 (coronene), dye 3 (coumarin 153), and dye 7 (4′-

hydroxybenzylidene-2,3-dimethylimidazolinone) are more sensitive to the amount of HF exchange, and the most accurate functional is the range separated hybrid LC-BLYP. For dyes 3 and 7, this is a consequence of the $S_1 \leftarrow S_0$ transition involving an intramolecular charge transfer event. It was not possible to optimize the bright excited state of dye 7 using BLYP due to the presence of a nearby spurious charge transfer transition. On the other hand, dye 2 involves excitations of electrons in a highly delocalized π system, where traditional XC functionals perform poorly in general. Asymptotic corrections to the XC functional are known to be important for describing charge transfer excitations[42,103−113] and potential energy surfaces.[114,115]

The measured absorption spectrum[93] of dye 1 shows a weakly allowed $S_1 \leftarrow S_0$ transition and strongly allowed $S_2 \leftarrow S_0$ transition. Fluorescence for dye 1 was measured by exciting to the S_2 state, but the observed spectrum is largely obscured by the overlapping phosphorescence spectrum. On the basis of the low intensity and proximity to the absorption feature of the S_1 state, it is likely that the emission comes from the S_1 state rather than S_2, so the excited state optimization in the TDDFT calculations was performed for the S_1 state. The intense phosphorescence and overlapping onset of the S_2 state absorption with the S_1 state absorption make it difficult to determine the Stokes shift experimentally. We therefore simulated the absorption and fluorescence including vibronic effects to estimate the Stokes shift.

Figure 3a shows the simulated absorption and fluorescence spectra of dye 1. Simulations for both the syn and anti conformations of the aldehyde were used, although the anti conformation is ∼0.10 eV (774 cm^{-1}) more stable. The spectra were simulated with the 0−0 peak of the vibronic progression for absorption and fluorescence coincident with the experimental measurements (26 040 and 26 015 cm^{-1}, respectively) for both the syn and anti conformations.[93] For the anti conformation, the absorption and fluorescence spectra show a progression in the carbonyl stretching frequency (1730 cm^{-1}). The peak of the absorption occurs between the third and fourth peaks, while the peak of fluorescence occurs at the third peak of the progression. This yields an estimated Stokes shift between 0.86 and 1.07 eV, in agreement with the values determined using the TDDFT optimization.

Figure 3b compares the simulated and measured fluorescence spectra of dye 1. The analysis presented in ref 93 determined
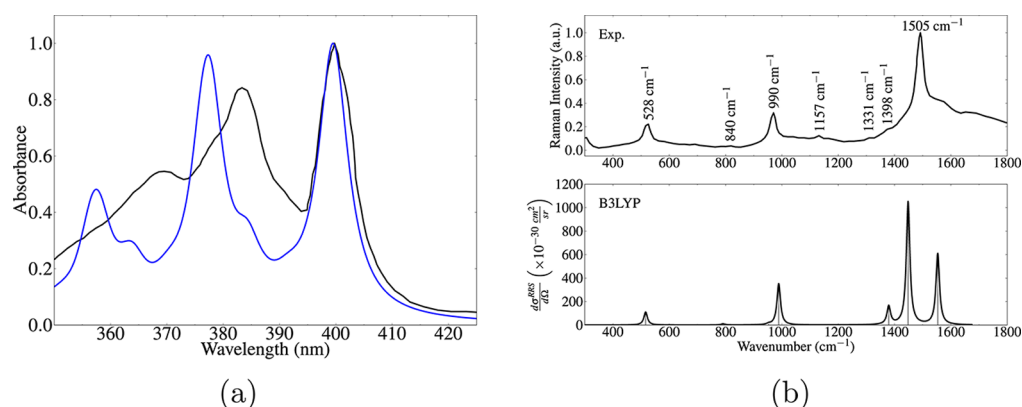
Figure 4. (a) Absorption spectrum for the $D_3 \leftarrow D_0$ transition of the phenoxyl radical complex simulated with B3LYP/aug-cc-pVDZ (blue line) in comparison to the experimental spectrum (black line) adapted from ref 124. (b) Simulated resonance Raman spectrum using B3LYP compared with the experimental spectrum[124] at 399 nm.

that the fluorescence almost entirely results from the anti conformation based on DFT calculated frequencies and the small amount of syn conformers at room temperature. Among the features marked by arrows in the measured fluorescence spectrum, the first, third, fifth, and sixth peaks can be explained by emission by the anti conformer. However, the fourth vibronic peak corresponds strongly with the syn conformer. This indicates that emission from both conformers is observed experimentally, so an isomerization process between the more stable anti conformer to the syn conformer likely occurs in the excited state.

4.2. Optical Processes of the Phenoxyl Radical. The phenoxyl radical is a model system for investigating the tyrosyl radical,[116] which is important in biological processes such as the formation of deoxyribonucleotides,[117] water oxidation during photosynthesis,[118] and an important intermediate in the oxidation of benzene.[119] Characterization of the phenoxyl radical often proceeds using spectroscopy due to its short lifetime. Simulated and experimental OPA[120−122] and RRS[54,122−124] have facilitated the understanding of the electronic and structural properties of the phenoxyl radical and enabled characterization of the tyrosyl radical also.

Tripathi and Schuler characterized the phenoxyl radical and its isotopomers using OPA and RRS in aqueous solution (see Figure 4).[123,124] The RRS measured on resonance with the $^2B_1 \leftarrow {}^2A_2$ transition possesses a broad background between 1300 and 1900 cm^{-1} (between 420 and 440 nm) and is argued to result from weak fluorescence of the phenoxyl radical. On the basis of the experimental OPA and RRS spectra, the Stokes shift of the phenoxyl radical is 0.21 eV. Table 3 presents simulated results compared with the experimental Stokes shift.

Table 3. Absorption Maxima, Emission Maxima, and Stokes Shift (S.S.) for the Phenoxyl Radical Resulting from the $D_3 \leftarrow D_0$ ($^2B_1 \leftarrow {}^2A_2$) Transition Using BLYP, LC-BLYP, B3LYP, and CAM-B3LYP Using the 6-31G* Basis Set[a]

method	Abs.	Em.	S.S.
BLYP	3.37	3.07	0.30
B3LYP	3.59	3.27	0.32
CAM-B3LYP	3.81	3.44	0.37
LC-PBE	3.85	3.45	0.40
Exp.	3.11	2.90	0.21

[a]Values are given in eV. The experimental data is from ref 124.

In general, the magnitudes of the differences between simulated and experimental Stokes shifts are comparable to those of section 4.1. However, it is found that the BLYP functional gives the best agreement with experimental data. The overestimation of the Stokes shift by the different functionals may be attributed to the neglect of solvent effects on the absorption and emission.[49,125,126]

Figure 4 presents the simulated OPA and RRS spectra for the $D_3 \leftarrow D_0$ transition of the phenoxyl radical compared with the experimental spectra of ref 124. The simulated OPA spectrum yields many of the observed features in the vibrational progression, although the features are blueshifted from the positions observed in the experiment. This behavior was also observed in a recent study by Santoro et al. regardless of whether Duschinsky rotations were included in the simulation.[122] Tentatively, we attribute this disagreement to interactions between the solvent and phenoxyl radical that are not included in the present model. Such effects, including both explicit and bulk interactions, which have been included in several previous studies of absorption and emission processes, have been demonstrated to be important.[46,49,101,102] The RRS spectrum (Figure 4b) shows good agreement with the experimental spectrum. The four most prominent features (528, 990, 1398, and 1505 cm^{-1}) are vibronically coupled to the electronic transition, and this is captured in the simulation. These results are confirmation that scattering from the phenoxyl radical results from an A term (Franck−Condon) mechanism. Weaker features labeled in the experimental spectrum are absent in the simulations and have been demonstrated to arise from Herzberg−Teller coupling terms that are not included here.[122] The peak at 1585 cm^{-1} in the simulation is not well resolved in the experiment due to the broad fluorescence background in that region of the RRS spectrum.

4.3. Charge Transfer in a Molecular Host−Guest Complex. The host−guest complex of tetrathiafulvalene (TTF) with cyclobis(paraquat-p-phenylene) (CBPQT^{4+}) is a model system for studying analyte binding processes. This complex is shown in Figure 5. It was demonstrated previously that resonance Raman scattering is a powerful analytical technique for determining binding energies while also obtaining structural information about complexation.[127] The formation of the TTF⊂CBPQT^{4+} complex results in an excited state located at 865 nm, which is caused by an intermolecular charge transfer (CT) state between TTF and CBPQT^{4+}. The simulated
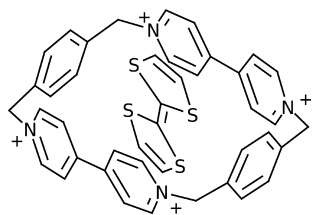
Figure 5. Structure of the TTF⊂CBPQT⁴⁺ host−guest complex.

4.4. Simulated Spectra for Rhodamine 6G.
The fluorescent dye rhodamine 6G (R6G, shown in Figure 7) has

Figure 7. Structure of the fluorescent dye rhodamine 6G.

resonance Raman spectrum of the complex using BP86 was shown to result in intense features at approximately 500 cm^{-1}, attributed to the poor description of CT states with traditional DFT XC functionals. Here, we simulate resonance Raman spectra of the complex using the global hybrid B3LYP and range separated hybrid LC-ωPBE, which we have previously used to study photon driven CT events.[115]

Figure 6a shows the simulated absorption spectra of TTF⊂CBPQT⁴⁺. While B3LYP calculations find the absorption maximum to be 1.13 eV, LC-ωPBE determines the absorption maximum to be 2.09 eV. The experimental absorption maximum is 1.43 eV, so both calculated results are shifted such that the absorption maximum coincides with the experimental absorption maximum. Simulations with both XC functionals are capable of reproducing the experimental spectrum. However, the blue edge of the spectrum is underestimated.

Figure 6b illustrates the simulated resonance Raman spectra of the complex in comparison with the experimental spectrum. Both B3LYP and LC-ωPBE yield spectra comparable to experimental data, in contrast with the simulated BP86 spectrum in ref 127. HF exchange is therefore important for describing relative peak intensities in resonance Raman spectra. Strong features are observed at 471 cm^{-1} (TTF S atom ring breathing), 701 cm^{-1} (TTF C−S stretch), 1477 cm^{-1} (CBPQT⁴⁺ CH₂ scissoring), and 1637 cm^{-1} (CBPQT⁴⁺ pyridyl C−C stretching). For the simulated B3LYP spectrum, the mode at 1637 cm^{-1} is overestimated significantly. The same mode is underestimated slightly with LC-ωPBE. In general, the relative peak intensities using LC-ωPBE are in better agreement with experimental results, illustrating the importance of range separated hybrids for predicting vibronic features for CT states.
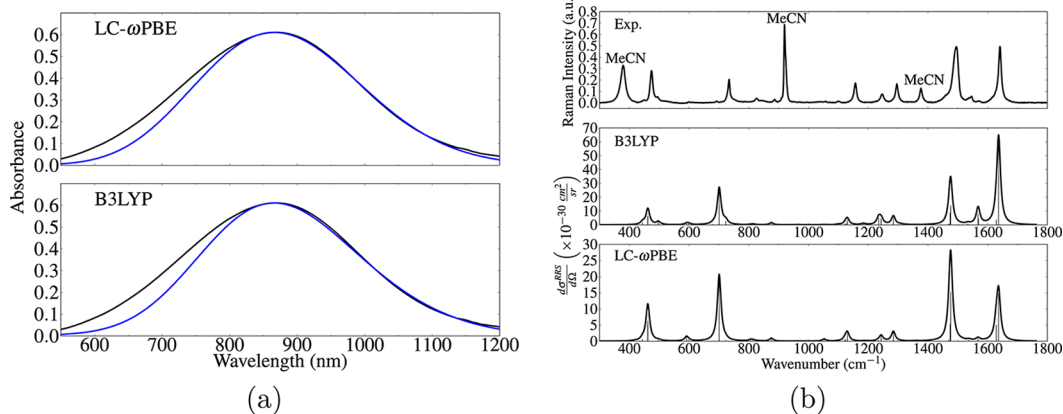
been the center of many recent Raman scattering studies. TDDFT calculations of static and frequency-dependent polarizabilities were used to simulate nonresonant Raman and RRS, allowing the resonance enhancement ($\sim 10^5$) to be quantified.[128] It has been demonstrated that vibronic effects are important for capturing the correct relative peak intensities with RRS for R6G also.[79−81] TDDFT simulations with vibronic coupling have also been instrumental in understanding the complicated nature of resonance hyper-Raman scattering and surface-enhanced hyper-Raman scattering in R6G.[15,83,129]

We examined the strongly allowed $S_1 \leftarrow S_0$ transition with different XC functionals. Because each functional yields a different excitation energy, the OPA spectra are shifted so that the absorption maximum is aligned with the experimental spectrum. Figure 8 shows the simulated OPA spectrum with each functional. The functionals are split into four panels and show very different behaviors. For the local and semilocal functionals (LDA, BP86, and PBE), the spectra show a main peak with a vibronic shoulder at approximately 490 nm. Each functional in this case overestimates the intensity of the vibronic shoulder compared to the experimental spectrum.

The global hybrid (B3LYP and PBE0) functionals show very similar behavior. Both functionals significantly improve the description of the vibronic feature in the OPA spectrum. Interestingly, the long-range corrected hybrid (CAM-B3LYP, BNL, LC-PBE, LC-PBE0, LC-ωPBE, LC-ωPBEh) functionals are less consistent in their description of the OPA spectrum. BNL and LC-PBE0 yield poor spectra in comparison with experimental results, where the vibronic structure is more intense than the main peak leading to a broad feature. This is contrasted by the other long-range corrected hybrids, which

Figure 6. (a) Absorption spectra of the TTF⊂CBPQT⁴⁺ complex simulated with B3LYP and LC-ωPBE in comparison to the experimental spectrum (black line). (b) Simulated resonance Raman spectra using B3LYP and LC-ωPBE compared with the experimental spectrum[127] at 785 nm. Acetonitrile solvent lines in the resonance Raman spectrum are designated with MeCN.
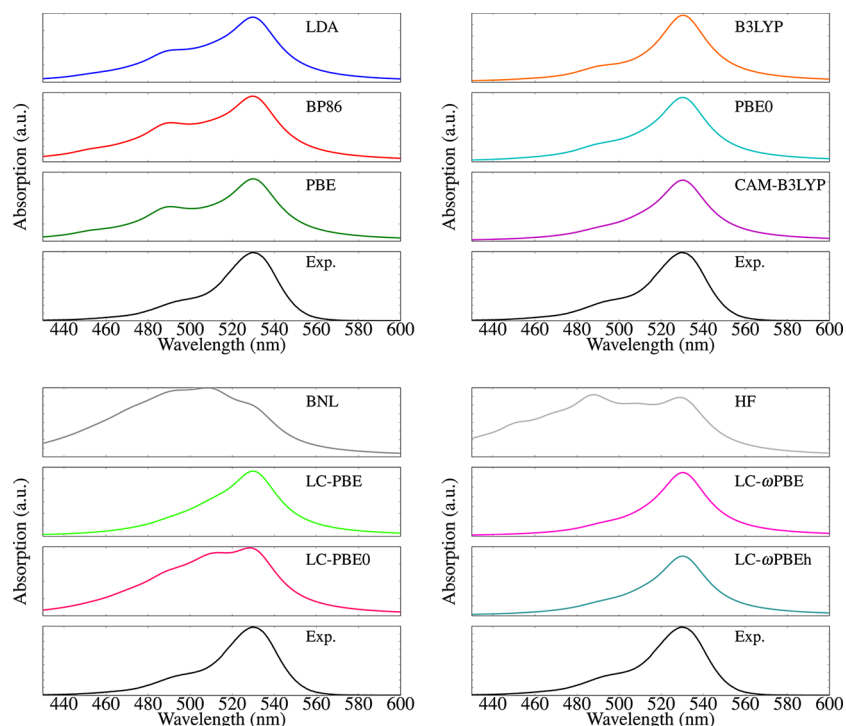
Figure 8. Absorption spectra of rhodamine 6G using different XC functionals in comparison with experimental data.[130] Spectra are shifted so that the absorption maximum coincides with the experimental absorption maximum.
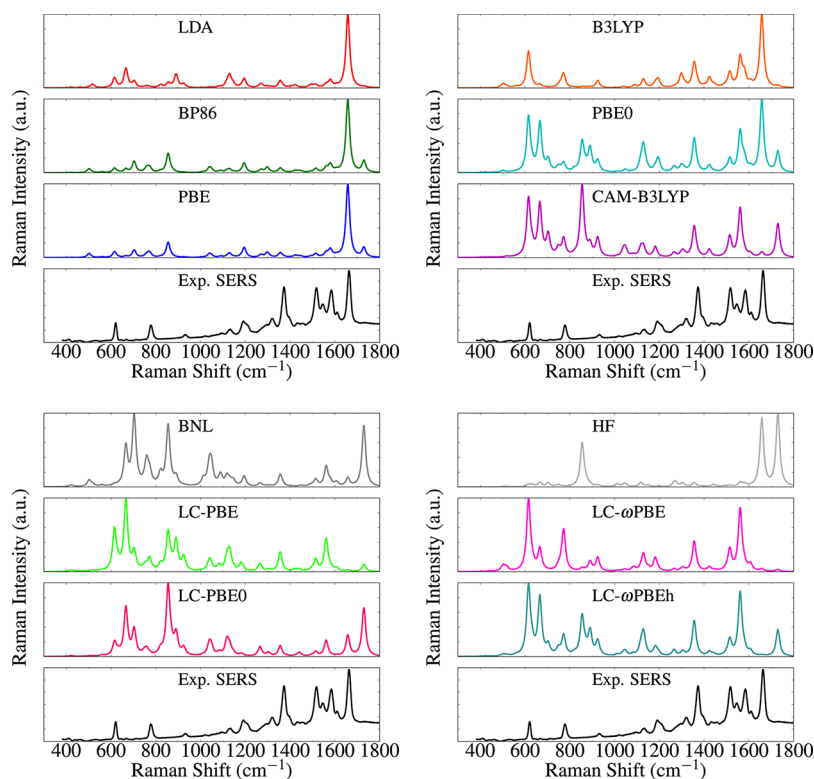
Figure 9. Resonance Raman spectra of rhodamine 6G using different XC functionals. Simulations are performed assuming a wavelength of 514.5 nm.

have spectra comparable to the global hybrid functionals. It was thought, because long-range corrected hybrids generally use 100% HF exchange at large interelectronic separations, that a pure HF calculation might elaborate on deficiencies of some of these functionals. The HF calculation gives similar results to BNL and LC-PBE0, demonstrating the connection between

these methods. Surprisingly, however, CAM-B3LYP, LC-PBE, LC-ωPBE, and LC-ωPBEh do not possess problems in the OPA spectrum, so further investigation requires the vibrational information provided by RRS.

Figure 9 shows the RRS spectra of rhodamine 6G using the same functionals. For comparison, the experimental surface-

enhanced Raman scattering (SERS) spectrum is shown, which is measured at 514.5 nm. Although many peaks are present in the SERS spectrum, we focus on the modes at 616, 772, 1356, 1515, 1579, and 1656 cm^{-1}. Aside from the mode at 1663 cm^{-1}, the local and semilocal functionals underestimate the intensity of every feature in the SERS spectrum. The global hybrid, B3LYP, which we have previously used in other studies to obtain good agreement with experimental results,[15,83] compares very well with the experimental spectrum. However, the modes at 1373 and 1518 cm^{-1} are underestimated.

Although the global hybrids PBE0 and B3LYP use similar amounts of HF exchange (25% and 20%, respectively), the simulated spectra from both functionals vary substantially below 1000 cm^{-1}. Many features that are not observed in the SERS spectrum appear in the PBE0 spectrum. Examining the semilocal functionals BP86 and PBE, we observe that the spectra are comparable. It may be surprising then that B3LYP and PBE0 give very different looking spectra, since B3LYP uses the same exchange functional as BP86 and PBE0 uses the same exchange functional as PBE. Tentatively, we attribute these differences to sensitivity of the different XC functionals to the structure and normal modes used in the calculations as well as to the basis sets. For different functionals, the ground state optimized structure and normal modes do not need to be identical, and this may impact the quality of the response properties we calculate. Further work is being done to quantify the effect of the geometry and basis set choice for large molecules.

RRS spectra using the long-range corrected hybrids and HF are split into two groups. The functionals CAM-B3LYP, LC-PBE, LC-ωPBE, and LC-ωPBEh give similar spectra. Recall that these functionals also yielded reasonable OPA spectra in comparison to the experimental data (Figure 8). Although the ratios of the peaks in the RRS spectra are sensitive to the functional used, it appears that the observed modes are identical for these functionals. The other functionals, BNL, LC-PBE0, and HF, were characterized by poor agreement with the experimental OPA spectrum. From the RRS spectra, these functionals each have a large peak at 855 and 1730 cm^{-1}. The broad vibronic features in the OPA spectra for BNL, LC-PBE0, and HF are likely associated with the 1730 cm^{-1} mode, since that feature differs from the other functionals.

To better understand the analytical gradient results with B3LYP, we compare them to a RRS spectrum simulated with numerical gradients. Figure 10a and c show the comparison of the analytical and numerical gradient simulations with a simulation using parameters from ref 59 (Figure 10d). We see that the same modes are predicted to couple to the $S_1 \leftarrow S_0$ transition in the analytical and numerical methods, although the relative intensities differ. The analytical gradient method yields a spectrum comparable to the RRS spectrum reported in a previous study by our group.[79] In comparison to the experimental RRS spectrum, the data generated from numerical gradients are in better agreement (the peak at ~375 cm^{-1} in the experimental spectrum was not included in the simulations). A possible explanation for this behavior is that the analytical gradient depends on two perturbations (the external electric field and change in geometry), meaning that it is a quadratic response property. Previous work has demonstrated that quadratic response properties are sensitive to the size of the basis set,[131,132] so the gradients and vibronic coupling parameters may change significantly depending on the quality of the basis set. Guthmuller and Champagne[80,81] similarly
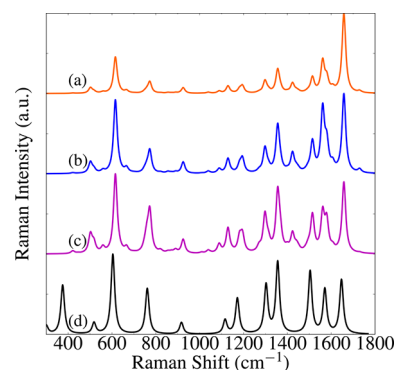
Figure 10. Resonance Raman spectra of rhodamine 6G calculated with B3LYP. The figures are (a) analytical gradient, (b) analytical gradient with displacement of the 1656 mode scaled by 70%, (c) numerical gradient, and (d) simulated RRS with parameters from ref 59. Simulations were performed at 532 nm.

found that numerical evaluation of the vibronic coupling parameters using B3LYP/6-311G* gives good agreement with experimental spectra. It is expected that analytical gradients are more accurate than numerical gradients, so the better agreement using numerical gradients with experimental results is likely fortuitous.

Table 4 shows a comparison of the dimensionless displacements from the numerical and analytical methods. In general,

Table 4. Dimensionless Displacements for Important Modes in Rhodamine 6G Using Numerical and Analytical Gradients Determined Using B3LYP^a

frequency (cm^{-1})	numerical Δ	analytical Δ	absolute difference (%)
616	−0.24	−0.24	0.00 (0.0)
772	−0.16	−0.12	0.04 (33.3)
1129	−0.12	−0.10	0.02 (20.0)
1182	0.09	0.07	0.02 (28.6)
1195	−0.10	−0.09	0.01 (10.0)
1298	−0.14	−0.12	0.02 (16.7)
1356	0.18	0.17	0.01 (6.0)
1515	−0.14	−0.13	0.01 (7.7)
1561	0.14	0.19	0.05 (26.3)
1579	0.12	0.11	0.01 (9.1)
1656	−0.20	−0.31	0.11 (35.5)

^{a}Percent differences are determined relative to the analytical gradient result.

the parameters are similar. The modes at 1561 and 1656 cm^{-1} have the largest absolute deviations in the two methods. These differences are comparable to those calculated between the analytical and numerical gradient methods by Petrenko and Neese for *trans*-hexatriene with the same functional.[53,78]

To obtain better agreement between the two methods, we tried scaling the intensity of the 1656 mode (Figure 10b). By reducing the intensity of that mode, the analytical gradient spectrum becomes comparable to the numerical one. Although the spectra still do not overlap perfectly, the agreement between both methods is improved by scaling the 1656 mode by 70%. Small differences in the other relative peak intensities are caused by the variations in the dimensionless displacements (Table 4).

4.5. Timings. In Table 5, CPU times for a TDDFT energy + gradient and TDDFT gradient are presented for the P2TA

Table 5. CPU Timings (s) for a TDDFT Energy + Gradient of P2TA (Dye 10 in Figure 2) and TDDFT Gradient of the First Excited State[a]

N_{CPUs}	TDDFT energy + gradient	TDDFT gradient
32	3260	1477
64	1714	742
128	969	377
256	687	224

[a]The TDDFT energy was calculated for the lowest five states. Calculations were performed using B3LYP/6-31G* (864 basis functions).

molecule (dye 10 in Figure 2) using the B3LYP functional and 6-31G* basis set (864 basis functions). Although the implementation described here is still a development version, good scaling is observed up to 128 processors for this molecule. These timing tests were performed on the Chinook computer system at EMSL, PNNL.[133]

5. CONCLUSION

In this work, we have presented an implementation of analytical excitation energy gradients within the TDDFT framework. As part of our validation, we calculated the Stokes shifts for a range of organic dye molecules using a diverse set of XC functionals including traditional DFT functionals, global hybrids, and range-separated hybrids. We also simulated the OPA and RRS of the well-studied dye molecule rhodamine 6G, phenoxyl radical, and a molecular host−guest complex (TTF⊂CBPQT^{4+}). Our calculations demonstrate the importance of analytic TDDFT gradients for efficient computation of vibronic coupling parameters. Our results show that the RRS depends strongly on the XC functional used and thus serves as a stringent benchmark of the accuracy of the XC functionals. For the molecule, rhodamine 6G, we observe that the best description of the potential energy surface is obtained using the global hybrid B3LYP functional. Surprisingly, we find that the long-range corrected functionals provide a rather poor description of the RRS of rhodamine 6G.

ASSOCIATED CONTENT

Ⓢ Supporting Information

Optimized structures of various dye molecules in the ground state using the B3LYP functional. This material is available free of charge via the Internet at http://pubs.acs.org/.

AUTHOR INFORMATION

Corresponding Authors

*E-mail: niri.govind@pnl.gov.
*E-mail: jensen@chem.psu.edu.

Notes

The authors declare no competing financial interest.

REFERENCES

(1) Morton, S. M.; Silverstein, D. W.; Jensen, L. *Chem. Rev.* **2011**, *111*, 3962−3994.

(2) Helgaker, T.; Coriani, S.; Jørgensen, P.; Kristensen, K.; Olsen, J.; Ruud, K. *Chem. Rev.* **2012**, *112*, 543−631.

(3) Champagne, B.; Plaquet, A.; Pozzo, J.-L.; Rodriguez, V.; Castet, F. *J. Am. Chem. Soc.* **2012**, *134*, 8101−8103.

(4) Kulesza, A.; Mitrić, R.; Bonačić-Koutecký, V. *J. Phys. Chem. A* **2009**, *113*, 3783−3788.

(5) Nielsen, K. A.; Sarova, G. H.; Martín-Gomis, L.; Stein, P. C.; Sanguinet, L.; Levillain, E.; Sessler, J. L.; Guldi, D. M.; Sastre-Santos, Á.; Jeppesen, J. O. *J. Am. Chem. Soc.* **2008**, *130*, 460−462.

(6) Yuan, H.; Chong, H.; Wang, B.; Zhu, C.; Liu, L.; Yang, Q.; Lv, F.; Wang, S. *J. Am. Chem. Soc.* **2012**, *134*, 13184−13187.

(7) Zhang, J.; Wong, K.-L.; Wong, W.-K.; Mak, N.-K.; Kwong, D. W. J.; Tam, H.-L. *Org. Biomol. Chem.* **2011**, *9*, 6004−6010.

(8) Uppal, R.; Ciesienski, K. L.; Chonde, D. B.; Loving, G. S.; Caravan, P. *J. Am. Chem. Soc.* **2012**, *134*, 10799−10802.

(9) Liu, Z.; Zhang, C.; He, W.; Qian, F.; Yang, X.; Gao, X.; Guo, Z. *New J. Chem.* **2010**, *34*, 656.

(10) Picot, A.; D'Aléo, A.; Baldeck, P. L.; Grichine, A.; Duperray, A.; Andraud, C.; Maury, O. *J. Am. Chem. Soc.* **2008**, *130*, 1532−1533.

(11) Egolf, D. S.; Waterland, M. R.; Myers Kelley, A. *J. Phys. Chem. B* **2000**, *104*, 10727−10737.

(12) Kleinman, S. L.; Ringe, E.; Valley, N.; Wustholz, K. L.; Phillips, E.; Scheidt, K. A.; Schatz, G. C.; Van Duyne, R. P. *J. Am. Chem. Soc.* **2011**, *133*, 4115−4122.

(13) Kamarchik, E.; Krylov, A. I. *J. Phys. Chem. Lett.* **2011**, *2*, 488−492.

(14) Petrenko, T.; Krylova, O.; Neese, F.; Sokolowski, M. *New J. Phys.* **2009**, *11*, 015001.

(15) Milojevich, C. B.; Silverstein, D. W.; Jensen, L.; Camden, J. P. *J. Am. Chem. Soc.* **2011**, *133*, 14590−14592.

(16) Runge, E.; Gross, E. K. U. *Phys. Rev. Lett.* **1984**, *52*, 997−1000.

(17) Casida, M. E. In *Recent Advances in Density Functional Methods, Part I*; Chong, D. P., Ed.; World Scientific: Singapore, 1995; Recent Advances in Computational Chemistry, Vol. *1*, Chapter 5, pp 155−192.

(18) Casida, M. E. In *Recent Developments and Applications of Modern Density Functional Theory*; Seminario, J. M., Ed.; Elsevier: Amsterdam, 1996; Theoretical and Computational Chemistry, Vol. *4*, pp 391−439.

(19) Hirata, S.; Head-Gordon, M. *Chem. Phys. Lett.* **1999**, *314*, 291.

(20) Stratmann, R. E.; Scuseria, G. E.; Frisch, M. J. *J. Chem. Phys.* **1998**, *109*, 8218−8224.

(21) Masunov, A.; Tretiak, S. *J. Phys. Chem. B* **2004**, *108*, 899−907.

(22) Zhao, L. L.; Jensen, L.; Schatz, G. C. *Nano Lett.* **2006**, *6*, 1229−1234.

(23) Aikens, C. M. *J. Phys. Chem. A* **2009**, *113*, 10811−10817.

(24) Marques, M. A. L.; Gross, E. K. U. *Annu. Rev. Phys. Chem.* **2004**, *55*, 427−455.

(25) Casida, M.; Huix-Rotllant, M. *Annu. Rev. Phys. Chem.* **2012**, *63*, 287−323.

(26) Ray, K.; DeBeer George, S.; Solomon, E. I.; Wieghardt, K.; Neese, F. *Chem.—Eur. J.* **2007**, *13*, 2783−2797.

(27) Stener, M.; Fronzoni, G.; de Simone, M. *Chem. Phys. Lett.* **2003**, *373*, 115−123.

(28) Besley, N. A.; Asmuruf, F. A. *Phys. Chem. Chem. Phys.* **2010**, *12*, 12024−12039.

(29) Liang, W.; Fischer, S. A.; Frisch, M. J.; Li, X. *J. Chem. Theory Comput.* **2011**, *7*, 3540−3547.

(30) Lopata, K.; Van Kuiken, B. E.; Khalil, M.; Govind, N. *J. Chem. Theory Comput.* **2012**, *8*, 3284−3292.

(31) Van Kuiken, B. E.; Valiev, M.; Daifuku, S. L.; Bannan, C.; Strader, M. L.; Cho, H.; Huse, N.; Schoenlein, R. W.; Govind, N.; Khalil, M. *J. Phys. Chem. A* **2013**, *117*, 4444−4454.

(32) Van Caillie, C.; Amos, R. D. *Chem. Phys. Lett.* **1999**, *308*, 249−255.

(33) Van Caillie, C.; Amos, R. D. *Chem. Phys. Lett.* **2000**, *317*, 159−164.

(34) Amos, R. D. *Chem. Phys. Lett.* **2002**, *364*, 612−615.

(35) Burcl, R.; Amos, R. D.; Handy, N. C. *Chem. Phys. Lett.* **2002**, *355*, 8−18.

(36) Furche, F.; Ahlrichs, R. *J. Chem. Phys.* **2002**, *117*, 7433−7447.

(37) Rappoport, D.; Furche, F. *J. Chem. Phys.* **2005**, *122*, 064105.

(38) Hutter, J. *J. Chem. Phys.* **2003**, *118*, 3928−3934.

(39) Odelius, M.; Laikov, D.; Hutter, J. *J. Mol. Struct.: THEOCHEM* **2003**, *630*, 163−175.

(40) Seth, M.; Mazur, G.; Ziegler, T. *Theor. Chem. Acc.* **2011**, *129*, 331−342.

(41) Petrenko, T.; Kossmann, S.; Neese, F. *J. Chem. Phys.* **2011**, *134*, 054116.

(42) Chiba, M.; Tsuneda, T.; Hirao, K. *J. Chem. Phys.* **2006**, *124*, 144106.

(43) Nguyen, K. A.; Day, P. N.; Pachter, R. *Int. J. Quantum Chem.* **2010**, *110*, 2247−2255.

(44) Liu, F.; Gan, Z.; Shao, Y.; Hsu, C.-P.; Dreuw, A.; Head-Gordon, M.; Miller, B. T.; Brooks, B. R.; Yu, J.-G.; Furlani, T. R.; Kong, J. *Mol. Phys.* **2010**, *108*, 2791−2800.

(45) Liu, J.; Liang, W. Z. *J. Chem. Phys.* **2011**, *134*, 044114.

(46) Scalmani, G.; Frisch, M. J.; Mennucci, B.; Tomasi, J.; Cammi, R.; Barone, V. *J. Chem. Phys.* **2006**, *124*, 094107.

(47) Marenich, A. V.; Cramer, C. J.; Truhlar, D. G.; Guido, C. A.; Mennucci, B.; Scalmani, G.; Frisch, M. *J. Chem. Sci.* **2011**, *2*, 2143−2161.

(48) Si, D.; Li, H. *J. Chem. Phys.* **2010**, *133*, 144112.

(49) Minezawa, N.; Silva, N. D.; Zahariev, F.; Gordon, M. S. *J. Chem. Phys.* **2011**, *134*, 054111.

(50) Doltsinis, N. L.; Kosov, D. S. *J. Chem. Phys.* **2005**, *122*, 144101.

(51) Ismail-Beigi, S.; Louie, S. G. *Phys. Rev. Lett.* **2003**, *90*, 076401.

(52) Sitt, A.; Kronik, L.; Ismail-Beigi, S.; Chelikowsky, J. R. *Phys. Rev. A* **2007**, *76*, 054501.

(53) Petrenko, T.; Neese, F. *J. Chem. Phys.* **2012**, *137*, 234107.

(54) Ma, H.; Liu, J.; Liang, W. *J. Chem. Theory Comput.* **2012**, *8*, 4474−4482.

(55) Savarese, M.; Aliberti, A.; De Santo, I.; Battista, E.; Causa, F.; Netti, P. A.; Rega, N. *J. Phys. Chem. A* **2012**, *116*, 7491−7497.

(56) Avila Ferrer, F. J.; Cerezo, J.; Stendardo, E.; Improta, R.; Santoro, F. *J. Chem. Theory Comput.* **2013**, *9*, 2072−2082.

(57) Kupfer, S.; Guthmuller, J.; González, L. *J. Chem. Theory Comput.* **2012**, *9*, 543−554.

(58) Poizat, O.; Sourisseau, C. *J. Phys. Chem.* **1984**, *88*, 3007−3014.

(59) Shim, S.; Stuart, C. M.; Mathies, R. A. *ChemPhysChem* **2008**, *9*, 697−699.

(60) Angeloni, L.; Smulevich, G.; Marzocchi, M. P. *J. Raman Spectrosc.* **1979**, *8*, 305−310.

(61) Lueck, H. B.; McHale, J. L.; Edwards, W. D. *J. Am. Chem. Soc.* **1992**, *114*, 2342−2348.

(62) Ibrahim, M.; Xu, C.; Spiro, T. G. *J. Am. Chem. Soc.* **2006**, *128*, 16834−16845.

(63) Ruban, A. V.; Berera, R.; Ilioaia, C.; van Stokkum, I. H. M.; Kennis, J. T. M.; Pascal, A. A.; van Amerongen, H.; Robert, B.; Horton, P.; van Grondelle, R. *Nature* **2007**, *450*, 575−578.

(64) Balakrishnan, G.; Jarzecki, A. A.; Wu, Q.; Kozlowski, P. M.; Wang, D.; Spiro, T. G. *J. Phys. Chem. B* **2012**, *116*, 9387−9395.

(65) Markel, F.; Ferris, N. S.; Gould, I. R.; Myers, A. B. *J. Am. Chem. Soc.* **1992**, *114*, 6208−6219.

(66) Lilichenko, M.; Tittelbach-Helmrich, D.; Verhoeven, J. W.; Gould, I. R.; Myers, A. B. *J. Chem. Phys.* **1998**, *109*, 10958−10969.

(67) Zong, Y.; McHale, J. L. *J. Chem. Phys.* **1997**, *106*, 4963−4972.

(68) Zong, Y.; McHale, J. L. *J. Chem. Phys.* **1997**, *107*, 2920−2929.

(69) Valiev, M.; Bylaska, E.; Govind, N.; Kowalski, K.; Straatsma, T.; Van Dam, H.; Wang, D.; Nieplocha, J.; Apra, E.; Windus, T.; de Jong, W. *Comput. Phys. Commun.* **2010**, *181*, 1477−1489.

(70) Heller, E. J. *J. Chem. Phys.* **1975**, *62*, 1544−1555.

(71) Heller, E. J. *J. Chem. Phys.* **1976**, *64*, 63−73.

(72) Lee, S.-Y.; Heller, E. J. *J. Chem. Phys.* **1979**, *71*, 4777−4788.

(73) Tannor, D. J.; Heller, E. J. *J. Chem. Phys.* **1982**, *77*, 202−218.

(74) Heller, E. J. *Acc. Chem. Res.* **1981**, *14*, 368−375.

(75) Heller, E. J.; Sundberg, R.; Tannor, D. *J. Phys. Chem.* **1982**, *86*, 1822−1833.

(76) Duschinsky, F. *Acta Phys. U.R.S.S.* **1937**, *7*, 551−556.

(77) Neugebauer, J.; Hess, B. A. *J. Chem. Phys.* **2004**, *120*, 11564.

(78) Petrenko, T.; Neese, F. *J. Chem. Phys.* **2007**, *127*, 164319.

(79) Kane, K. A.; Jensen, L. *J. Phys. Chem. C* **2010**, *114*, 5540−5546.

(80) Guthmuller, J.; Champagne, B. *ChemPhysChem* **2008**, *9*, 1667−1669.

(81) Guthmuller, J.; Champagne, B. *J. Phys. Chem. A* **2008**, *112*, 3215−3223.

(82) Jarzęki, A. A. *J. Phys. Chem. A* **2009**, *113*, 2926−2934.

(83) Milojevich, C. B.; Silverstein, D. W.; Jensen, L.; Camden, J. P. *J. Phys. Chem. C* **2013**, *117*, 3046−3054.

(84) Reiher, M.; Neugebauer, J.; Hess, B. A. *Z. Phys. Chem.* **2003**, *217*, 91−103.

(85) Silverstein, D. W. Applications of Time-dependent Quantum Mechanics to Resonantly-enhanced Linear and Nonlinear Optical Processes. Ph.D. thesis, The Pennsylvania State University, University Park, PA, 2013.

(86) Silverstein, D. W.; Jensen, L. TDSPEC: Time-Dependent Spectroscopic Simulations of Linear and Nonlinear Optical Processes. The Pennsylvania State University, University Park, PA, 2011.

(87) Grimme, S. *J. Comput. Chem.* **2006**, *27*, 1787−1799.

(88) Besler, B. H.; Scuseria, G. E.; Scheiner, A. C.; Schaefer, H. F. *J. Chem. Phys.* **1988**, *89*, 360−366.

(89) Stanton, J. F.; Watts, J. D.; Bartlett, R. J. *J. Chem. Phys.* **1991**, *94*, 404−413.

(90) Scott, A. P.; Radom, L. *J. Phys. Chem.* **1996**, *100*, 16502−16513.

(91) Alecu, I. M.; Zheng, J.; Zhao, Y.; Truhlar, D. G. *J. Chem. Theory Comput.* **2010**, *6*, 2872−2887.

(92) Kowalczyk, T.; Tsuchimochi, T.; Chen, P.-T.; Top, L.; Voorhis, T. V. *J. Chem. Phys.* **2013**, *138*, 164101.

(93) Itoh, T. *J. Mol. Struct.* **2010**, *261*, 53−58.

(94) Itoh, T. *J. Mol. Struct.* **2008**, *252*, 115−120.

(95) Ernsting, N. P.; Asimov, M.; Schäfer, F. P. *Chem. Phys. Lett.* **1982**, *91*, 231−235.

(96) Haucke, G.; Graness, G. *Angew. Chem., Int. Ed.* **1995**, *34*, 67−68.

(97) Creemers, T. M. H.; Lock, A. J.; Subramaniam, V.; Jovin, T. M.; Völker, S. *Nat. Struct. Biol.* **1999**, *6*, 557−560.

(98) Ma, Y.; Rohlfing, M.; Molteni, C. *J. Chem. Theory Comput.* **2009**, *6*, 257−265.

(99) Williams, R.; Goldsmith, G. J. *J. Chem. Phys.* **1963**, *39*, 2008−2011.

(100) Eastwood, D.; Edwards, L.; Gouterman, M.; Steinfeld, J. *J. Mol. Struct.* **1966**, *20*, 381−390.

(101) Jacquemin, D.; Planchat, A.; Adamo, C.; Mennucci, B. *J. Chem. Theory Comput.* **2012**, *8*, 2359−2372.

(102) Silva, D. L.; Murugan, N. A.; Kongsted, J.; Rinkevicius, Z.; Canuto, S.; Ågren, H. *J. Phys. Chem. B* **2012**, *116*, 8169−8181.

(103) Lange, A. W.; Herbert, J. M. *J. Am. Chem. Soc.* **2009**, *131*, 3913−3922.

(104) Silverstein, D. W.; Jensen, L. *J. Chem. Phys.* **2010**, *132*, 194302.

(105) Govind, N.; Valiev, M.; Jensen, L.; Kowalski, K. *J. Phys. Chem. A* **2009**, *113*, 6041−6043.

(106) Jensen, L.; Govind, N. *J. Phys. Chem. A* **2009**, *113*, 9761−9765.

(107) Andzelm, J.; Rinderspacher, B. C.; Rawlett, A.; Dougherty, J.; Baer, R.; Govind, N. *J. Chem. Theory Comput.* **2009**, *5*, 2835−2846.

(108) Kowalski, K.; Krishnamoorthy, S.; Villa, O.; Hammond, J. R.; Govind, N. *J. Chem. Phys.* **2010**, *132*, 154103.

(109) Glaesemann, K. R.; Govind, N.; Krishnamoorthy, S.; Kowalski, K. *J. Phys. Chem. A* **2010**, *114*, 8764−8771.

(110) Lopata, K.; Govind, N. *J. Chem. Theory Comput.* **2011**, *7*, 1344−1355.

(111) Lopata, K.; Reslan, R.; Kowalska, M.; Neuhauser, D.; Govind, N.; Kowalski, K. *J. Chem. Theory Comput.* **2011**, *7*, 3686−3693.

(112) Refaely-Abramson, S.; Sharifzadeh, S.; Govind, N.; Autschbach, J.; Neaton, J. B.; Baer, R.; Kronik, L. *Phys. Rev. Lett.* **2012**, *109*, 226405.

(113) Stein, T.; Autschbach, J.; Govind, N.; Kronik, L.; Baer, R. *J. Phys. Chem. Lett.* **2012**, *3*, 3740−3744.

(114) Dreuw, A.; Head-Gordon, M. *J. Am. Chem. Soc.* **2003**, *126*, 4007−4016.

(115) Silverstein, D. W.; Jensen, L. *J. Chem. Theory Comput.* **2010**, *6*, 2845−2855.

(116) Sander, W.; Roy, S.; Polyak, I.; Ramirez-Anguita, J. M.; Sanchez-Garcia, E. *J. Am. Chem. Soc.* **2012**, *134*, 8222−8230.

(117) Engström, M.; Himo, F.; Gräslund, A.; Minaev, B.; Vahtras, O.; Ågren, H. *J. Phys. Chem. A* **2000**, *104*, 5149−5153.

(118) Nugent, J. H.; Ball, R. J.; Evans, M. C. *Biochim. Biophys. Acta* **2004**, *1655*, 217−221.

(119) Herbinet, O.; Husson, B.; Ferrari, M.; Glaude, P.-A.; Battin-Leclerc, F. *Proc. Combust. Inst.* **2013**, *34*, 297−305.

(120) Radziszewski, J. G.; Gil, M.; Gorski, A.; Spanget-Larsen, J.; Waluk, J.; Mróz, B. J. *J. Chem. Phys.* **2001**, *115*, 9733−9738.

(121) Dierksen, M.; Grimme, S. *J. Chem. Phys.* **2004**, *120*, 3544−3554.

(122) Santoro, F.; Cappelli, C.; Barone, V. *J. Chem. Theory Comput.* **2011**, *7*, 1824−1839.

(123) Tripathi, G.; Schuler, R. H. *Chem. Phys. Lett.* **1983**, *98*, 594−596.

(124) Tripathi, G. N. R.; Schuler, R. H. *J. Chem. Phys.* **1984**, *81*, 113.

(125) Doltsinis, N. L.; Markwick, P. R. L.; Nieber, H.; Langer, H. In *Challenges and Advances In Computational Chemistry and Physics*; Shukla, M. K., Leszczynski, J., Eds.; Springer: Netherlands, 2008; Vol. 5, pp 265−299.

(126) Gustavsson, T.; Bányász, Á.; Lazzarotto, E.; Markovitsi, D.; Scalmani, G.; Frisch, M. J.; Barone, V.; Improta, R. *J. Am. Chem. Soc.* **2005**, *128*, 607−619.

(127) Witlicki, E. H.; Hansen, S. W.; Christensen, M.; Hansen, T. S.; Nygaard, S. D.; Jeppesen, J. O.; Wong, E. W.; Jensen, L.; Flood, A. H. *J. Phys. Chem. A* **2009**, *113*, 9450−9457.

(128) Jensen, L.; Schatz, G. C. *J. Phys. Chem. A* **2006**, *110*, 5973−5977.

(129) Milojevich, C. B.; Silverstein, D. W.; Jensen, L.; Camden, J. P. *ChemPhysChem* **2011**, *12*, 101−103.

(130) Dixon, J. M.; Taniguchi, M.; Lindsey, J. S. *Photochem. Photobiol.* **2005**, *81*, 212−213.

(131) Sałek, P.; Vahtras, O.; Helgaker, T.; Ågren, H. *J. Chem. Phys.* **2002**, *117*, 9630−9645.

(132) Paterson, M. J.; Christiansen, O.; Pawlowski, F.; Jørgensen, P.; Hättig, C.; Helgaker, T.; Sałek, P. *J. Chem. Phys.* **2006**, *124*, 054322.

(133) Chinook computer system. See http://www.emsl.pnl.gov/capabilities/computing/msc/supercomputing/supercomputer.jsp.